Computer Physics Communications 316 (2025) 109772

Contents lists available at ScienceDirect

Computer Physics Communications

journal homepage: www.elsevier.com/locate/cpc

Computer Programs in Physics

An improved argument principle root-search method for modes of slab waveguides, optical fibers, and spheres

Sravya Rao [*,1], Parry Y. Chen [1], T. Grossinger, Yonatan Sivan

School of Electrical and Computer Engineering, Ben-Gurion University, Israel

ARTICLE INFO

The review of this paper was arranged by Prof. W. Jong

Keywords:
Complex root search
Argument principle method
Optical waveguide dispersion relation

ABSTRACT

We update our root-search method for transcendental equations. Our method is globally convergent and is guaranteed to locate all complex roots within a specified search domain, since it is based on Cauchy's residue theorem. We extend the implementation to treat the dispersion relations of slab waveguides and the resonances of a sphere, in addition to step-index fibers. We also implement other improvements, such as to the contour selection procedure and using non-dimensional search variables, to ensure the method remains reliable even in challenging parameter regimes. We also extend the algorithm to identify leaky modes in terms of propagation constant eigenvalue modes, revealing, to the first time to our knowledge, a discontinuity across the light line in the dispersion plot.

NEW VERSION PROGRAM SUMMARY

Program Title: disproots (Dispersion roots)
CPC Library link to program files: https://doi.org/10.17632/32297nv5kk.2
Licensing provisions: CC BY NC 3.0
Programming language: MATLAB
Journal reference of previous version: Comput. Phys. Commun. 214 (2017) 105.
Does the new version supersede the previous version?: Yes
Reasons for the new version: Even though the algorithm is theoretically guaranteed to locate all roots, our original implementation [1] is still liable to miss some of the roots at certain parameter regimes in the context of the optical waveguide dispersion relation. In this update, we make the algorithm more reliable. The other reason for this update is to extend the implementation of our algorithm to treat the dispersion relations of other waveguide geometries and applicability in determining the leaky modes in the context of propagation constant modes.
Summary of revisions: To ensure the method is reliable even in challenging parameter regimes, we make several revisions in the contour selection strategy like enlargement of the contour for lower-order roots, adapting the simple circular contours used previously [1] by elliptically-shaped contours and employing adaptive scheme for higher-order roots. Additionally, we also rescale the search variables in the context of the propagation constant when the spacing between roots is large. We further demonstrate the extension of the method to slab & sphere geometries, and computation of leaky modes.
Nature of problem: Locating the complex roots of a general transcendental equation is often a non-trivial task. Iterative methods such as Newton's method face numerous difficulties because the existence of roots with narrow and otherwise difficult attraction basins requires very accurate initial guesses to locate. Robust location of a complete set of roots thus becomes problematic. In optics, modes of a circular fiber are obtained from a transcendental equation, the dispersion relation. Several recent advancements in optics have necessitated its robust solution, including the fabrication of high index contrast fibers and analytical methods that expand radiating sources using eigenmodes.
Solution method: We employ the argument principle method, a robust globally convergent method guaranteed to locate all roots in the specified search domain. It is based on the Cauchy residue theorem, and projects the locations of the roots on to a polynomial basis. Unlike previous implementations of the argument principle method [2,3] and related methods [4], our implementation has two features vital for solving the fiber dispersion relation. It allows isolated singularities within the search domain, and allows the search domain to approach arbitrarily close to branch points without experiencing failure. Furthermore, our simple MATLAB implementation is designed to be easily modified and integrated for a variety of applications.

* Corresponding author.
E-mail address: sravya@post.bgu.ac.il (S. Rao).
[1] Equal contributors to this update.

https://doi.org/10.1016/j.cpc.2025.109772
Received 3 March 2025; Received in revised form 8 June 2025; Accepted 15 July 2025

Available online 22 July 2025
0010-4655/© 2025 The Author(s). Published by Elsevier B.V. This is an open access article under the CC BY-NC license (http://creativecommons.org/licenses/by-nc/4.0/).

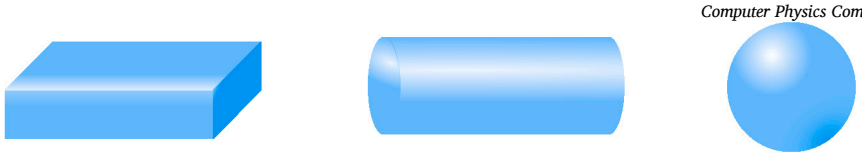

Fig. 1. The three geometries treated in this update: a slab waveguide with infinite translational symmetry in two dimensions, a circular fiber infinitely extended in one direction, and a sphere.

Additional comments including restrictions and unusual features: The specified search domain must be meromorphic, in other words be complex analytic containing at most isolated singularities. The locations and orders of these singularities must be known analytically, so we describe how they are determined for our fiber dispersion relation. Branch points and branch cuts must be avoided, though the search domain may be arbitrarily close. We exploit knowledge of our dispersion relation, specifically that roots are located close to singularities, to simplify the method.

References

[1] P.Y. Chen, Y. Sivan, Robust location of optical fiber modes via the argument principle method, Comput. Phys. Commun. 214 (2017) 105–116.
[2] L.C. Botten, M.S. Craig, R.C. McPhedran, Complex zeros of analytic functions, Comput. Phys. Commun. 29 (3) (1983) 245–259.
[3] P. Kravanja, M. Van Barel, O. Ragos, M.N. Vrahatis, F.A. Zafiropoulos, ZEAL: a mathematical software package for computing zeros of analytic functions, Comput. Phys. Commun. 124 (2–3) (2000) 212–232.
[4] C.J. Gillan, A. Schuchinsky, I. Spence, Computing zeros of analytic functions in the complex plane without using derivatives, Comput. Phys. Commun. 175 (4) (2006) 304–313.

1. Introduction

In this update, we revisit our original algorithm [1], where we implemented a robust, globally convergent argument principle root-search subroutine for transcendental equations. The algorithm is guaranteed to locate all roots within a specified search domain of the complex plane, since it is a globally convergent algorithm based on Cauchy's residue theorem. We applied the algorithm to treat the step-index optical fiber dispersion relation, i.e., to find dispersion curves (ω-frequency vs β-propagation constant [2,3], or β-modes in short) given a user-specified fiber radius and material dispersion relation. Free-to-use code was published alongside the original article [1]. The algorithm found the roots up to any desired order with minimal human supervision, and without any concerns of divergence with increased number of iterations [4]. The implementation can also search for permittivity as the eigenvalue, which is useful for defining the normal modes of open, unbounded systems [5–28].

The first purpose of this update is to enhance the reliability of our implementation in the context of optical waveguide dispersion relations. Even though the algorithm is theoretically guaranteed to locate all roots, our original implementation [1] is still liable to miss some of the roots. There are two possible reasons for this. Firstly, if the search domain is not specified to be large enough to encompass all the roots, then roots that stray deep into the complex plane will be missed. This can occur under certain parameter regimes. Secondly, the algorithm might fail due to the limitations of finite precision arithmetic when the search variable becomes very small or very large. In this update, we revise the algorithm to resolve these issues, yielding a more reliable implementation. These improvements are described in Section 2.1.

The second purpose of this update is to demonstrate its applicability to compute the leaky optical waveguide (β) modes, i.e., those for which the search variable is a complex propagation constant β; previously, we studied such modes only when the search variable was the (eigen-) permittivity. Such modes are encountered also in the context of the Schrödinger equation in the description of electron states whose energies are above the vacuum level [29]; the optical formulation adopted below reduces to this case for a fixed value of the frequency. Details of the leaky mode computation are presented in Section 2.2.

The third purpose of this update is to extend the implementation of our algorithm to compute the dispersion relations of slab waveguide and spherical scatterers, see Fig. 1. These structures yield simpler transcendental equations compared to step-index optical fiber, often resulting in more regular root distributions and simpler attraction basins. Thus, these root searches are perhaps less challenging and may be more amenable to simpler techniques, such as the locally convergent Newton's method. However, since the roots can lie in the complex plane, locally convergent techniques can still be unreliable, as their success depends heavily on good initial guesses. To ensure that no roots are missed, it remains beneficial to use our globally convergent algorithm. In Section 2.3, we demonstrate the implementation of the algorithm for a symmetric slab waveguide and for spherical geometries.

2. Novelities

2.1. Revisions to algorithm

Our root-search algorithm [1] was originally implemented to solve the transcendental equation governing the circular fiber, defined by

$$f_m \equiv \left(\frac{\mu_c}{\alpha_c a}\frac{J_m'(\alpha_c a)}{J_m(\alpha_c a)} - \frac{\mu_b}{\alpha_b a}\frac{H_m'(\alpha_b a)}{H_m(\alpha_b a)}\right)\left(\frac{\epsilon_c}{\alpha_c a}\frac{J_m'(\alpha_c a)}{J_m(\alpha_c a)} - \frac{\epsilon_b}{\alpha_b a}\frac{H_m'(\alpha_b a)}{H_m(\alpha_b a)}\right) - \left(\frac{m\beta}{k}\right)^2\left(\frac{1}{(\alpha_c a)^2} - \frac{1}{(\alpha_b a)^2}\right)^2 = 0. \tag{1}$$

Here, J_m denotes the Bessel function of the first kind, and H_m is the Hankel function of the first kind. The index m represents the angular variation of the field ($\sim e^{im\theta}$), a is the radius of the circular core, ϵ and μ are the relative permittivity and permeability of the core (denoted by subscript c) and background (b), k is the free space wavenumber, and β is the propagation constant along the fiber axis. The in-plane propagation constants α_c and α_b differ between the core and background,

$$\alpha_c^2 = k^2\epsilon_c\mu_c - \beta^2, \quad \alpha_b^2 = k^2\epsilon_b\mu_b - \beta^2. \tag{2}$$

In this implementation, the root search was carried out using either ϵ_c or β as the search variable, with the contour selection strategy guided by two key observations: (a) there exists one root for each singularity, counting multiplicities, and (b) these roots are often located in the vicinity of their respective singularities. We thus devised a simple strategy to enclose all the roots with a set of overlapping contours, with one contour centered on each singularity. This was specified in Eq. (14) of our original manuscript [1] and demonstrated there in Fig. 2. However, the strategy can fail under certain parameter regimes. For instance, in the long-wavelength limit ($ka < 1$) or when the index contrast is small, roots tend to deviate more significantly from their associated singularities, and the contours may no longer adequately enclose them. This deviation manifests along both the real and imaginary axes of the complex plane of search variables. While deviations along the real axis for higher-order roots are still captured by overlapping contours, the situation becomes tenuous for lower-order roots, as the first contour lacks a neighboring

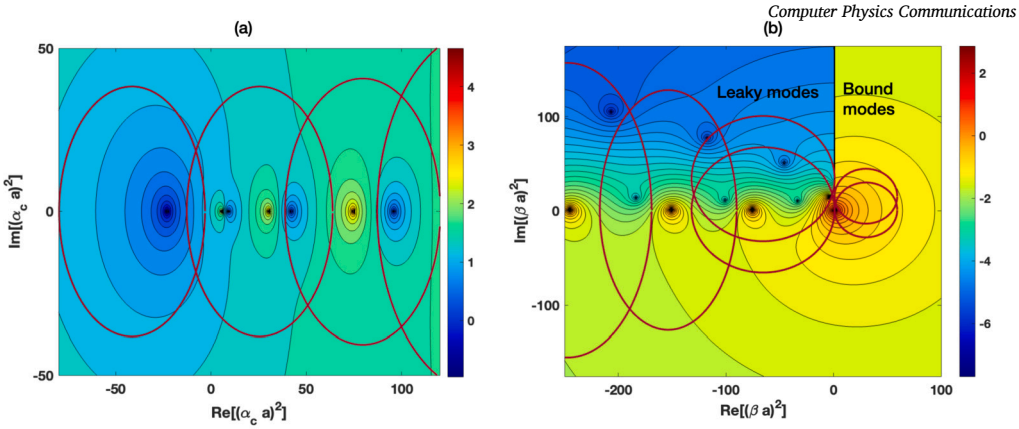

Fig. 2. Examples of the attraction basins and our revised contour selection strategy (magenta) for a circular fiber geometry. Horizontal and vertical axes represent real and imaginary parts of the complex search variable domain, while the color indicates the logarithmic magnitude of the transcendental equation (1) ($\log_{10}(|f(z)|)$; see equivalent figure in [1] for more details). Thus, the roots correspond to the deep blue regions and the singularities to the red regions. Plot (a) shows the attraction basin of the $(\alpha_c a)^2$ search variable, featuring an enlarged contour (the second from the left) that encloses the first two singularities, as described in Eq. (3). Another contour, the leftmost one defined in Eq. (4), is included to capture plasmonic roots that may drift further into the negative half of the complex plane. Plot (b) shows an example of an attraction basin in the $(\beta a)^2$ search variable where a branch point exists at $\beta^2 = k^2\epsilon_b\mu_b$ with a branch cut selected to extend towards $+i\infty$. (For interpretation of the colors in the figure(s), the reader is referred to the web version of this article.)

contour on one side to help capture roots. Deviations along the imaginary axis, which become increasingly pronounced at long wavelengths, affect roots of all orders and further complicate their capture. To address these challenges, we introduced the following updates to the algorithm.

First, we revised the method by replacing the original search variables, ϵ_c and β, with $(\alpha_c a)^2$ and $(\beta a)^2$, respectively. This rescaling reduces the sensitivity of the attraction basins of the transcendental equation (f_m) to changes in a, with the proximity of roots to their singularities now solely determined by the dimensionless product ka. In addition, we search for $(\alpha_c a)^2$ rather than $\alpha_c a$, for example, since the latter would result in a duplication of the complex search space. For the implementation of the argument principle method, we provide the explicit expressions of the derivatives of f_m with respect to the updated search variables in Appendix A.1.

We also revised our contour strategy for finding the first few roots, via a simple modification that has been tested to succeed even for challenging parameter regimes. In particular, we combine the first two contours into one large contour that covers a much larger region of the search space. Even so, this enlarged contour still does not enclose more than 6 roots, and thus does not present any difficulties for the numerically sensitive Newton's identities. This contour is displayed in Fig. 2. Specifically, we define the center and radius of this enlarged contour to be

$$\begin{aligned} c_1 &= \frac{3}{8}u_3 + \frac{1}{8}u_2 + \frac{1}{8}u_1 + \frac{3}{8}u_0, \\ r_1 &= \frac{3}{8}u_3 + \frac{1}{8}u_2 - \frac{1}{8}u_1 - \frac{3}{8}u_0. \end{aligned} \tag{3}$$

This equation uses the notation of Eq. (13) from the original manuscript [1], where u_k is the value of k-th singularity, and $u_0 = 2u_1 - u_2$. Additionally, in the context of $(\alpha_c a)^2$ as the search variable, the plasmonic root often drifts further into the negative half of the complex plane. To ensure its capture, we introduce an additional contour positioned along the negative real axis, adjacent to the enlarged first contour. For our purposes, we choose a contour defined by

$$\begin{aligned} c_p &= c_1 - \frac{3}{2}r_1, \\ r_p &= r_1. \end{aligned} \tag{4}$$

This additional contour can be further enlarged to cover more of the search space. This does not risk numerical difficulties, since the contour is not expected to enclose many roots, if at all, and is situated in a relatively featureless region of the search space. An example of this contour is displayed in Fig. 2(a). If necessary, the contour can be further enlarged to cover even areas with known roots and singularities by running the additional contour last, and deflating the additional contour of all known roots and singularities. This ensures that the additional contour will not contain more than 5 new roots, which is necessary for the stability of the Newton identities.

To handle deviations of roots along the imaginary axis, especially at long wavelengths, we employ elliptical contours as roots may wander much farther along the imaginary axis in comparison to the distance between consecutive singularities on the real axis, as shown in Fig. 2(b). Like the circularly-shaped contours used so far, elliptically-shaped contours are periodic, so the equidistant trapezoidal rule for numerical integration converges exponentially.

However, elliptical contours, like circular ones, are not particularly effective at preventing failure of our root-search subroutine when the contour is simply shrunk in an attempt to avoid branch points and branch cuts. Thus, we avoid placing elliptical contours adjacent to branch cuts. Instead, we use multiple shifted circular contours to collectively cover the area that would otherwise be enclosed by an elliptical contour.

To make the root search more robust, we also implement an adaptive scheme to search further deep into the imaginary axis of the complex plane until a root is found, i.e.,

$$\begin{aligned} c_k &= c_k \pm l * r_k, \\ r_k &= r_k. \end{aligned} \tag{5}$$

Here, l is an integer and its value is incremented until a root is found for every contour.

2.2. Computation of the leaky (β) modes

In the context of optical waveguide (β) modes, a transcendental equation such as Eq. (1) is traditionally used to describe bound modes, characterized by α_b having a positive imaginary part to ensure field decay away from the core. However, it is also suitable to describe leaky modes, which were not considered in our original implementation [1]. Leaky modes exhibit both a radiative nature (i.e., a non-zero real part of α_b) and leakage (i.e., a negative imaginary part of α_b, leading to exponential growth); the latter reflects the open (i.e., non-Hermitian) nature of the problem.

This treatment of leaky modes contrasts with the more traditional Hermitian description of the problem, which yields a continuum of ra-

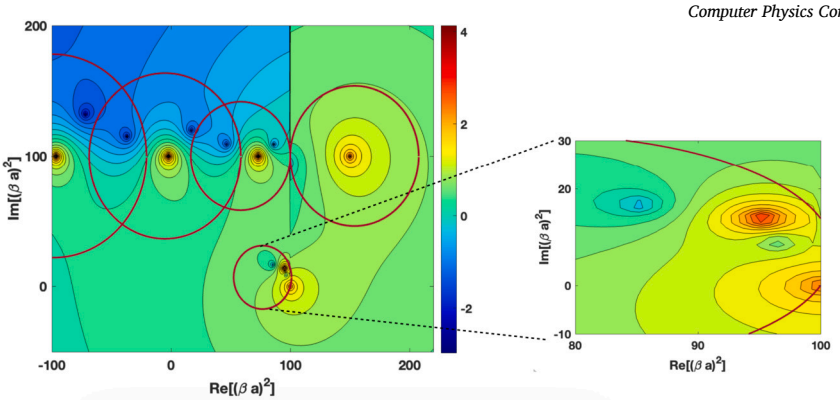

Fig. 3. Illustration of the scenario where a singularity arising from the Hankel function lies outside the region covered by the overlapping contours of the Bessel function zeros. An additional contour is introduced around the Hankel singularity, positioned below the overlapping Bessel function contours. The zoomed-in view shows the Hankel singularity and its surrounding roots in very close proximity, clearly demonstrating the algorithm's effectiveness in resolving roots within narrow attraction basins.

diative modes [30,31], i.e., modes for which there is no leakage (α_b is purely real). This Hermitian description requires a slightly more complicated spatial field profile (compared to Eq. (A.15) in Appendix A.2), one that also includes incoming waves in the background medium. Consequently, the field profiles and dispersion relations associated with the continuum of radiative modes are inconsistent with the conventional descriptions of bound modes.

An equivalent classification of bound and leaky modes can be made in terms of the eigenvalue β^2, relative to the light line of the background medium defined by the branch point $\beta^2 = k^2\epsilon_b\mu_b$ in the complex β^2 plane. Bound modes lie to the right of this branch point, where $\mathrm{Re}(\beta^2) > k^2\epsilon_b\mu_b$, while leaky modes lie to the left, where $\mathrm{Re}(\beta^2) < k^2\epsilon_b\mu_b$. Notably, because β^2 is generally complex, classification based solely on $\mathrm{Re}(\beta)$ is unreliable. This branch point is not only central to mode classification but also critical for the success of our method, as it must be avoided by root-searching contours. In particular, two branch cuts emanate from this branch point, originating separately from the square root function of α_b and the Hankel function. In MATLAB and most other numerical packages, branch cuts are positioned along the positive real axis in the complex domains of $(\beta a)^2$, which typically coincides with the region of the transcendental equation containing the bound modes. To prevent interference with the root-finding contours, it is therefore necessary to reposition these branch cuts.

The combined effect of the direction of α_b rotation and the choice of sign influences the mode properties, determining whether the modes exhibit the correct radiation and leakage behavior consistent with our problem formulation. Specifically, our original implementation [1], which targeted only bound modes, positioned the branch cuts along the negative imaginary axis and selected the negative square root branch. However, now that we are interested in leaky modes, we realize that this setup produces leaky modes with incoming wave boundary conditions, contradicting our intended outgoing wave formulation. Thus, our updated approach repositions the branch cuts along the positive imaginary axis and adopts the positive root branch to capture both bound and leaky modes of the transcendental equation with correct mode characterization. This is achieved by defining

$$\alpha_b = \sqrt{(k^2\epsilon_b\mu_b - \beta^2)e^{-i\pi/2}}\, e^{i\pi/4}, \quad H_m(\alpha_b a) = \frac{2}{\pi i^{m+1}} K_m(-i\alpha_b a). \tag{6}$$

With this configuration, the repositioned branch cuts naturally separate bound and leaky modes, as shown in Fig. 2(b).

In addition to the singularities treated in the original implementation, additional singularities may also arise from the complex zeros of the Hankel function, which on the principal branch lies just below the negative real axis and in an eye-shaped region below the origin in the $\alpha_b a$ plane [32]. During the repositioning of the branch cut along the imaginary axis, singularities arising from the Hankel function vanish in the region containing bound modes. The remaining singularities persist in the leaky mode region and tend to cluster tightly near the branch point, unlike the more widely distributed singularities associated with Bessel functions. These leaky-region singularities were previously ignored because the algorithm focused solely on bound modes. To accurately identify roots near the branch cut, it is necessary to include these singularities in the root count evaluation (i.e., for Eq. (6) in the original manuscript). Furthermore, there are scenarios where the roots in the vicinity of these singularities are not enclosed by the overlapping contours created by Bessel function zeros, as shown in Fig. 3. In this update, the algorithm has been extended to include Hankel singularities and, when necessary (as in Fig. 3), to introduce dedicated contours around them. Complex zeros of the Hankel function for azimuthal orders up to $m \leq 31$ are now precomputed and incorporated into the root-search module.

We demonstrate the computation of the leaky (β) modes for a numerical example of a non-magnetic circular fiber with core permittivity of $\epsilon_c = 12 + i$ embedded in a vacuum background medium ($\epsilon_b = 1$). In Fig. 4, we present the dispersion characteristics as β^2 versus k^2, instead of the traditional β versus k plot, to more clearly distinguish the modes based on their positions relative to the light lines. The plot shows $(ka)^2$ on the vertical axis, $\mathrm{Re}[(\beta a)^2]$ on the horizontal axis, and $\mathrm{Im}[(\beta a)^2]$ represented by color. The light lines of the background medium ($\beta^2 = \epsilon_b k^2$) and of the core medium ($\beta^2 = \epsilon_c k^2$) are shown as gray lines in the plots, where only the real part of the latter is depicted due to the complex nature of ϵ_c. Bound modes lie between the two light lines, while leaky modes are to the left of the background medium light line. We observe that the dispersion curves exhibit a discontinuity as they transition across the background medium light line, which can be attributed to the fact that bound and leaky modes lie on opposite sides of the branch cut (as shown in Fig. 2(b)). A related phenomenon is discussed in [33] in the context of hidden multi-sheeted resonances near branch cuts.

2.3. Implementation of the algorithm to other geometries

In this Section, we extend our root-search algorithm to general asymmetrically bound slab waveguide geometries (including the simplified symmetrical case) and sphere geometries.

2.3.1. Slab waveguide

We consider an asymmetrically bound slab waveguide geometry consisting of three layers: a guiding film layer, surrounded by a cover and a substrate, as shown in Fig. 5. We denote the permittivities and permeabilities of these layers as ϵ_f and μ_f, ϵ_c and μ_c, and ϵ_s and μ_s, respectively. The guiding layer is infinite in the y-z plane and finite along the x-axis, with thickness a.

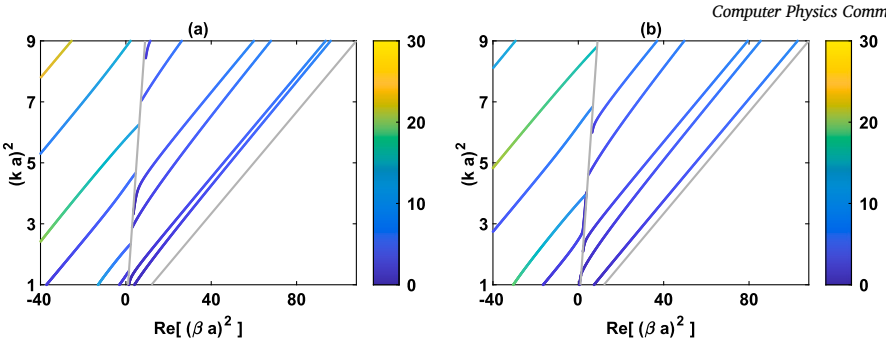

Fig. 4. Dispersion relations produced by our algorithm using complex $(\beta a)^2$ as the search variable for a circular fiber with core permittivity $\epsilon_c = 12 + i$ embedded in a vacuum background medium, where the core radius a is normalized to 1; $\mathrm{Im}[(\beta a)^2]$ is represented by color. Plot (a) shows modes corresponding to the angular order $m = 0$, and plot (b) is for $m = 1$ order. The leftmost gray line in each plot represents the vacuum (background medium) light line, while the other gray line corresponds to $\beta^2 = 12k^2$.

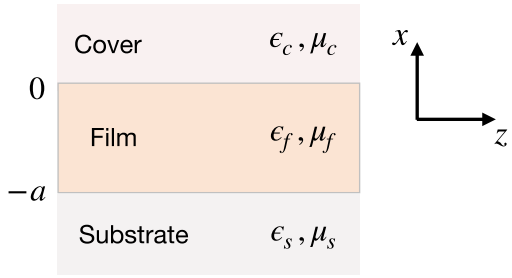

Fig. 5. Schematic of slab waveguide geometry shown in $x - z$ plane, with y-axis pointing out of the paper.

In this slab waveguide geometry, both transverse electric (TE) and transverse magnetic (TM) modes are supported. We treat these in turn. First, the transcendental equation of TE modes (f^{TE}) is given by [2]

$$f^{\mathrm{TE}} \equiv \frac{\alpha_f^2 + \alpha_c \alpha_s}{\alpha_f} \tan(\alpha_f a) + i(\alpha_c + \alpha_s) = 0, \tag{7}$$

where the transverse propagation constant α_j along the x-axis in regions $j \in c, f, s$ (cover, film, and substrate, respectively) is defined as

$$\alpha_j^2 = k^2 \epsilon_j \mu_j - \beta^2. \tag{8}$$

Here, k is the wavenumber in free space and β is the in-plane propagation constant along the z-direction. In this transcendental equation, we can set either $(\beta a)^2$ or $(\alpha_f a)^2$ as the eigenvalue or search variable.

Similarly, the transcendental equation for TM modes is given by

$$f^{\mathrm{TM}} \equiv \frac{\alpha_f^2 \epsilon_c \epsilon_s + \epsilon_f^2 \alpha_c \alpha_s}{\alpha_f \epsilon_f} \tan(\alpha_f a) + i(\epsilon_c \alpha_s + \epsilon_s \alpha_c) = 0. \tag{9}$$

We obtain the derivatives to the dispersion relations (7) and (9) in Appendix B.1, which are needed for the argument principle method.[2] Next, we demonstrate the numerical example of our algorithm for the slab waveguide for both search variables: $(\beta a)^2$ and $(\alpha_f a)^2$.

We demonstrate the numerical example of the algorithm for $(\beta a)^2$ as an eigenvalue for a symmetrical slab waveguide with guiding layer permittivity of $\epsilon_f = 12 + i$, and vacuum cover and substrate layers. We show dispersion relations (β^2 vs k^2) of TE and TM modes of this slab waveguide in Fig. 6, with $\mathrm{Re}[(\beta a)^2]$ along the horizontal axis and $\mathrm{Im}[(\beta a)^2]$ represented by color. The light lines of the substrate and cover coincide, given by $\beta^2 = k^2$ (vacuum light line), while the light line of the guiding film layer is $\beta^2 = \mathrm{Re}(\epsilon_f) k^2$; both are shown as gray lines in the dispersion plots. Since a branch cuts arises in the slab waveguide geometry due to the substrate and cover regions, we observe discontinuities in the dispersion curves across the vacuum light line, similar to what was observed in fibers in Section 2.2.

Next, we compute the permittivity modes. In this case, k and the permittivities of the substrate and cover are fixed; the propagation constant β is the independent variable of the dispersion relation, and the guiding film layer's permittivity ϵ_f is the dependent variable. Unlike in [1], here ϵ_f is determined by treating $(\alpha_f a)^2$ as the search variable. We show the dispersion relations for this case in Fig. 7. The only relevant light lines are those of the substrate and cover regions, which, in this example, are both vacuum; thus, they coincide, and this vacuum light line ($\beta = k$) appears as a vertical line in the dispersion plot since k is fixed. The bound modes exist to the right of the light line and always have real ϵ_f, while the leaky modes exist to the left of the light line and have complex ϵ_f. Since branch-cuts don't emerge in the transcendental equations (7) and (9) for $(\alpha_f a)^2$ search variable, the dispersion curves do not show any discontinuities across the vacuum light line.

The explicit expressions for the field profiles of such permittivity modes are given in Appendix B.2.

2.3.2. Spheres

We now turn to solve the transcendental equations for the modes of a sphere. The relevant parameters are the radius a, free-space wavenumber k, background permittivity ϵ_b. The modes can have two polarizations: TE, where the component of the electric field along the radial direction is zero, and TM, where the radial magnetic field is zero. Each of these modes is generated by separate dispersion relation equations:

TM:

$$f_l^{(\mathrm{TM})}(x) \equiv \frac{x j_l'(x)}{j_l(x)} - \frac{x_b h_l^{(1)\prime}(x_b)}{h_l^{(1)}(x_b)} = 0, \tag{10}$$

TE:

$$f_l^{(TE)}(x) \equiv \frac{1}{x^2}\left(1 + \frac{x j_l'(x)}{j_l(x)}\right) - \frac{1}{k_b^2}\left(1 + \frac{x_b h_l^{(1)\prime}(x_b)}{h_l^{(1)}(x_b)}\right) = 0. \tag{11}$$

Here, $x = \sqrt{\epsilon} ka$, j_l and $h_l^{(1)}$ are the spherical Bessel and spherical Hankel functions of the first kind of order l, and the prime denotes differentiation with respect to the entire argument. For a given polar order l and polarization ($F = TM$ or TE), we get an infinite sequence of roots which are enumerated by the radial order n, as mentioned in Appendix C, no additional information from the angular dependence affect the eigenvalues.

From repeated numerical experimentation, we observe that, as found for wire modes in [1], all the photonic roots in the $f_l^{(\mathrm{TM})}$ case are relatively close to their neighboring singularities (spherical Bessel function zeroes). Thus, the locations of the singularities, known analytically, provide guideposts for the locations of the roots and the center of the

[2] As pointed out in our earlier work [1, Eq. (10)], the use of the derivative of the dispersion relations is convenient, but not a necessity.

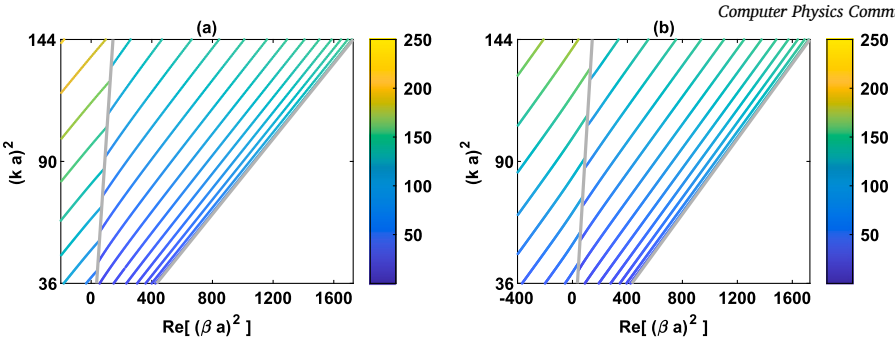

Fig. 6. Dispersion relations of modes of the symmetric slab waveguide, produced by our algorithm with complex $(\beta a)^2$ as the search variable, with $\mathrm{Im}[(\beta a)^2]$ represented by color. Plot (a) is of TE modes, and plot (b) shows TM modes for a guiding film layer of $\epsilon_f = 12 + i$ and vacuum background. The guiding film layer thickness a is normalized to 1. The gray line on the left of each figure indicates the light line of vacuum (i.e., $\beta^2 = k^2$), while the other gray line corresponds to $\beta^2 = 12k^2$. The modes between the two light lines are bound modes, i.e., their fields are evanescent in the background (i.e., in the cover and substrate layers). The modes above the first light line are leaky modes, i.e., their fields grow exponentially in the background.

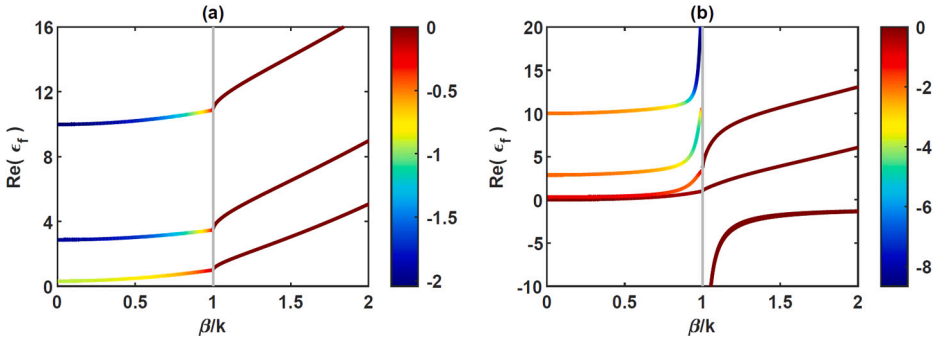

Fig. 7. Dispersion relations of eigenpermittivity modes of symmetrical slab waveguide determined using $(\alpha_f a)^2$ search variable. The results are shown in terms of ϵ_f of slab, with $\mathrm{Im}(\epsilon_f)$ indicated by color. Plot (a) is of TE modes, and plot (b) shows TM modes for a wave-number $k = 2$, with a guiding film layer thickness a normalized to 1, and vacuum in both substrate and cover regions. The vertical gray line indicates the light line of vacuum, and the bound modes with only real ϵ_f exist to the right of the light line, while leaky modes with complex ϵ_f exist to the left of the light line.

contours. However, the TE polarization has a special root that can be far from the singularities (for small spheres ($ka \ll 1$), it is a plasmonic root) or close to other root. In case it is beside other roots may cause the surrounding roots to move away or toward the closer singularity and could lead to troublesome features such as closely spaced roots, sharp resonances, and the presence of singularities near the roots, all of which can hinder the reliability and completeness of root-finding processes of $f_l^{(TE)}$. The special TE root has the largest imaginary absolute value. Only after finding all the other roots, we use a large contour to find it (this contour may contain more than two roots).

In both the TM and TE cases, we choose to use circular contours, which are the simplest to implement. In many cases, overlapping circles help us to cover the same root twice and give the method another opportunity to converge to the root using another initial guess. In some rare cases, we can use a smaller contour around the previous initial guess for the Newton-Raphson method that did not converge to a root.

In the $f_l^{(TE)}$ case, we observe that the roots of $f_l^{(TE)}$ are close to the roots of $f_0^{(TE)}$, therefore we locate the center of contour between these roots. We can easily find the roots of $f_0^{(TE)}$ using the Newton-Raphson method with an initial guess close to the singularities of $f_0^{(TE)}$.

Once again, to apply the argument principle method, we require the derivatives of (10) and (11), which are provided in Appendix C.1. As for the geometries studied above, the algorithm can be applied for either frequency or permittivity modes.

Fig. 8 shows the behavior of the eigenpermittivities of a sphere as a function of ka (where k is a constant). Each line represents a different n index, where l is constant ($l = 1$). One can see that the TE eigenvalues are all positive, and their real and imaginary parts decrease monotonically with growing radius. The behavior of the TM eigenvalues is similar, except for the $n = 1$ case, for which the eigenvalue becomes negative (i.e., plasmonic, $\epsilon_{nl}^{TM} \approx -2$) and purely real for small radii ($ka < 0.1$).

3. Outlook

We have described various improvements and extensions of our argument principle root-search applied to various generic optical structures. We specifically demonstrated propagation constant (β) and permittivity modes, but our algorithm can also be applied to frequency modes [34] (aka resonant states [35]). In addition to the usefulness of the algorithms detailed above per se, they also provide a convenient starting point for perturbation techniques (in the context of resonant state expansions [35] or re-expansion [17–19]). They can also be extended to simple geometries with more sophisticated physics, such as for systems with anisotropic, nonlocal [36–41] or non-reciprocal response. Finally, our algorithm can also be applied for the computation of electron wavefunctions in an arbitrary potential in atomic calculations [29]. All these potential directions would be explored in future research.

CRediT authorship contribution statement

Sravya Rao: Writing – original draft, Software, Methodology, Formal analysis, Conceptualization. **Parry Y. Chen:** Writing – original draft, Software, Formal analysis, Conceptualization. **T. Grossinger:** Conceptualization, Formal analysis, Software, Writing – original draft. **Yonatan Sivan:** Writing – review & editing, Supervision.

Declaration of competing interest

The authors declare the following financial interests/personal relationships which may be considered as potential competing interests:

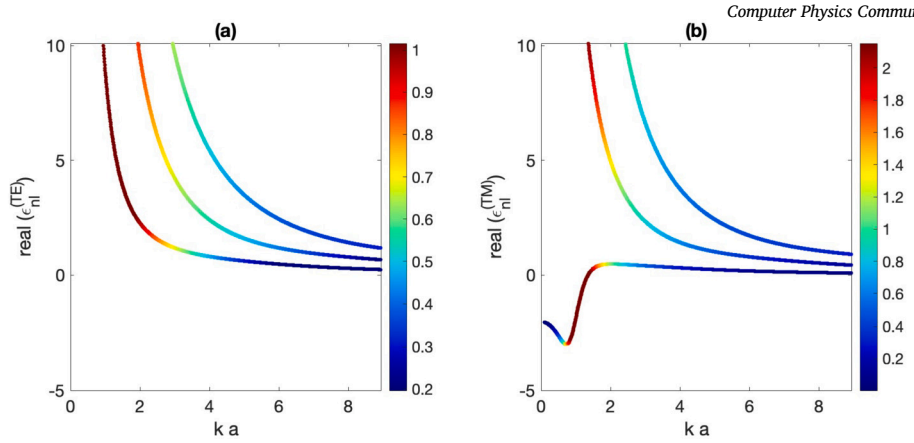

Fig. 8. Dispersion relations of eigenpermittivity modes of a sphere determined using (ka) search variable (where k is a constant). The y axis represents the real value of ϵ_{nl}, while $|(\mathrm{Im}(\epsilon_{nl})|$ is indicated by color. Each line represents different n index ($n = 1..3$), where l is constant ($l = 1$). Plot (a) is of TE modes, and plot (b) shows TM modes in a vacuum background.

Sravya Rao reports financial support was provided by Israel Science Foundation. Yonatan Sivan reports financial support was provided by Israel Science Foundation. Sravya Rao reports financial support was provided by German Research Foundation. Yonatan Sivan reports financial support was provided by German Research Foundation. If there are other authors, they declare that they have no known competing financial interests or personal relationships that could have appeared to influence the work reported in this paper.

Acknowledgements

S. R. and Y. S. were partially funded by Israel Science Foundation (ISF) grant no. 340/2020 and DFG (Deutsche Forschungsgemeinschaft – Middle East Collaboration) grant no. WE 5815/5-1.

Appendix A. Circular fiber geometry

In this Appendix, we present the analytical derivatives of the transcendental equation for circular fibers, which are required for our root-search algorithm, along with the corresponding field profiles associated with the roots.

A.1. Derivatives of transcendental equation

We evaluate the derivatives used by the argument principle and Newton's methods for both $(\alpha_c a)^2$ and $(\beta a)^2$ search variables. For notational simplicity, we introduce new symbols for the transcendental equation (1),

$$R_m^J = \frac{J_m'(\alpha_c a)}{\alpha_c a J_m(\alpha_c a)}, \qquad R_m^H = \frac{H_m'(\alpha_b a)}{\alpha_b a H_m(\alpha_b a)}. \tag{A.1}$$

Thus, the transcendental equation (1) can be rewritten as

$$f_m = (\epsilon_c R_m^J - \epsilon_b R_m^H)(\mu_c R_m^J - \mu_b R_m^H) - \left(\frac{m\beta}{k}\right)^2 \left(\frac{1}{(\alpha_c a)^2} - \frac{1}{(\alpha_b a)^2}\right)^2. \tag{A.2}$$

We first compute the derivative of f_m with respect to $(\alpha_c a)^2$, given by

$$\begin{aligned}\frac{\partial f_m}{\partial(\alpha_c a)^2} =& \left(\frac{\partial \epsilon_c}{\partial(\alpha_c a)^2} R_m^J + \epsilon_c \frac{\partial R_m^J}{\partial(\alpha_c a)^2}\right)(\mu_c R_m^J - \mu_b R_m^H) \\ &+ (\epsilon_c R_m^J - \epsilon_b R_m^H)\mu_c \frac{\partial R_m^J}{\partial(\alpha_c a)^2} + \frac{2m^2\beta^2}{(\alpha_c a)^4 k^2}\left(\frac{1}{(\alpha_c a)^2} - \frac{1}{(\alpha_b a)^2}\right),\end{aligned} \tag{A.3}$$

where

$$\frac{\partial \epsilon_c}{\partial(\alpha_c a)^2} = \frac{1}{(ka)^2 \mu_c}. \tag{A.4}$$

This expression follows from the relation $\alpha_c^2 + \beta^2 = k^2 \mu_c \epsilon_c$. In addition,

$$\frac{\partial R_m^J}{\partial(\alpha_c a)^2} = -\frac{1}{2(\alpha_c a)^2}\left[1 + 2R_m^J - \frac{J_{m+1}(\alpha_c a) J_{m-1}(\alpha_c a)}{J_m^2(\alpha_c a)}\right], \tag{A.5}$$

which is derived using the Bessel function's defining differential equation.

Next, we obtain the derivative of f_m with respect to $(\beta a)^2$, yielding

$$\begin{aligned}\frac{\partial f_m}{\partial(\beta a)^2} =& \left(\epsilon_b \frac{\partial R_m^H}{\partial(\alpha_b a)^2} - \epsilon_c \frac{\partial R_m^J}{\partial(\alpha_c a)^2}\right)(\mu_c R_m^J - \mu_b R_m^H) \\ &+ \left(\mu_b \frac{\partial R_m^H}{\partial(\alpha_b a)^2} - \mu_c \frac{\partial R_m^J}{\partial(\alpha_c a)^2}\right)(\epsilon_c R_m^J - \epsilon_b R_m^H) \\ &- \left(\frac{m}{ka}\right)^2 \left(\frac{1}{(\alpha_c a)^2} - \frac{1}{(\alpha_b a)^2}\right)^2 \left(1 + 2\left(\frac{\beta a}{\alpha_c a}\right)^2 + 2\left(\frac{\beta a}{\alpha_b a}\right)^2\right),\end{aligned} \tag{A.6}$$

where the chain rule was used along with the identity

$$\frac{\partial(\alpha_j a)^2}{\partial(\beta a)^2} = -1, \qquad j \in \{c, b\}. \tag{A.7}$$

Since the Hankel functions satisfy identities analogous to those of the Bessel functions, the expression of derivative $\partial R_m^H / \partial(\alpha_b a)^2$ can be obtained by substituting $\alpha_c \to \alpha_b$, $R_m^J \to R_m^H$ and $J_m(\alpha_c a) \to H_m(\alpha_b a)$ in Eq. (A.5).

A.2. Fiber mode field profiles

In this Appendix, we provide explicit expressions for the eigenmode fields of a step-index circular fiber, along with the normalization constants for both ϵ_c and β modes. The mode fields are expressed in the cylindrical coordinate system (ρ, θ, z), and they take a separable form

$$\boldsymbol{E}(\rho,\theta,z) = A\,\boldsymbol{e}(\rho) e^{im\theta} e^{i\beta z}, \quad \boldsymbol{H}(\rho,\theta,z) = A\,\boldsymbol{h}(\rho) e^{im\theta} e^{i\beta z}. \tag{A.8}$$

Here, A denotes the normalization constant (also referred to as the mode amplitude), and the vectors $\boldsymbol{e}(\rho)$ and $\boldsymbol{h}(\rho)$ represent the radial variation of the electric and magnetic fields, respectively. Their axial components,

$e_z(\rho)$ and $h_z(\rho)$, are sufficient to reconstruct the full vectors, as the transverse (ρ and θ) components can be obtained via[3]

$$\begin{aligned} e_r(\rho) &= \frac{i\beta}{\alpha_j^2}\frac{\partial e_z}{\partial \rho} - \frac{mk\mu_j}{\alpha_j^2\rho}h_z, \qquad e_\theta(\rho) = \frac{-m\beta}{\alpha_j^2\rho}e_z - \frac{ik\mu_j}{\alpha_j^2}\frac{\partial h_z}{\partial \rho}, \\ h_r(\rho) &= \frac{i\beta}{\alpha_j^2}\frac{\partial h_z}{\partial \rho} + \frac{mk\epsilon_j}{\alpha_j^2\rho}e_z, \qquad h_\theta(\rho) = \frac{-m\beta}{\alpha_j^2\rho}h_z + \frac{ik\epsilon_j}{\alpha_j^2}\frac{\partial e_z}{\partial \rho}, \end{aligned} \tag{A.9}$$

where $j \in \{c, b\}$ denotes the region (core or background, respectively), and the parameters α_j, μ_j, and ϵ_j take values specific to that region. In the above expressions, the mode indices (i.e., the subscripts m and n which denote the azimuthal and radial orders) are omitted to maintain generality across both ϵ_c and β modes. The indices are introduced in the following subsections for quantities that depend explicitly on the corresponding eigenvalue.

A.2.1. ϵ_c modes

We now introduce the mode indices mn to the eigenvalue (i.e., $\epsilon_{c,mn}$) and its dependent quantities: $\alpha_{c,mn}$, normalization constant A_{mn}, full fields ($\boldsymbol{E}_{mn}$, $\boldsymbol{H}_{mn}$), and radial field profiles ($\boldsymbol{e}_{mn}$, $\boldsymbol{h}_{mn}$). Thus, Eq. (A.8) takes the form

$$\begin{aligned} \boldsymbol{E}_{mn}(\rho,\theta,z) &= A_{mn}\,\boldsymbol{e}_{mn}(\rho)e^{im\theta}e^{i\beta z}, \\ \boldsymbol{H}_{mn}(\rho,\theta,z) &= A_{mn}\,\boldsymbol{h}_{mn}(\rho)e^{im\theta}e^{i\beta z}. \end{aligned} \tag{A.10}$$

The expression of the axial (z) components of $\boldsymbol{e}_{mn}$, $\boldsymbol{h}_{mn}$ are given by

$$\begin{aligned} e_{z,mn} &= f_{mn}(\rho), \\ h_{z,mn} &= H_{0,mn} f_{mn}(\rho), \end{aligned} \tag{A.11}$$

where

$$f_{mn}(\rho) = \begin{cases} \dfrac{J_m(\alpha_{c,mn}\rho)}{J_m(\alpha_{c,mn}a)} & \text{for} \quad r \le a \quad \text{(core)}, \\ \dfrac{H_m(\alpha_b\rho)}{H_m(\alpha_b a)} & \text{for} \quad r > a \quad \text{(background)}, \end{cases} \tag{A.12}$$

and

$$H_{0,mn} = \left(\frac{1}{\alpha_{c,mn}^2} - \frac{1}{\alpha_b^2}\right) \frac{m\beta}{ka\left[\dfrac{J_m'(\alpha_{c,mn}a)}{\alpha_{c,mn}J_m(\alpha_{c,mn}a)} - \dfrac{H_m'(\alpha_b a)}{\alpha_b H_m(\alpha_b a)}\right]}. \tag{A.13}$$

The normalization constants A_{mn} for $\epsilon_{c,mn}$ modes are given by

$$A_{mn} = \sqrt{\frac{1}{2\pi\int_0^a \left(-e_{r,mn}^2 + e_{\theta,mn}^2 + e_{z,mn}^2\right) r\,dr}}, \tag{A.14}$$

where this expression follows from the bi-orthogonality condition of the eigenpermittivity modes [6,16]. The transverse components $e_{r,mn}$ and $e_{\theta,mn}$ are obtained by substituting the axial components $e_{z,mn}$ and $h_{z,mn}$ into the expressions given in (A.9).

A.2.2. β modes

Similarly, we introduce the mode indices mn for the eigenvalue β_{mn} and its associated quantities: $\alpha_{c,mn}$, $\alpha_{b,mn}$, A_{mn}, fields ($\boldsymbol{E}_{mn}$, $\boldsymbol{H}_{mn}$), and radial field profiles ($\boldsymbol{e}_{mn}$, $\boldsymbol{h}_{mn}$). Accordingly, Eq. (A.8) becomes

$$\begin{aligned} \boldsymbol{E}_{mn}(\rho,\theta,z) &= A_{mn}\,\boldsymbol{e}_{mn}(\rho)e^{im\theta}e^{i\beta_{mn} z}, \\ \boldsymbol{H}_{mn}(\rho,\theta,z) &= A_{mn}\,\boldsymbol{h}_{mn}(\rho)e^{im\theta}e^{i\beta_{mn} z}. \end{aligned} \tag{A.15}$$

The axial components of $\boldsymbol{e}_{mn}$, $\boldsymbol{h}_{mn}$ are expressed as

$$\begin{aligned} e_{z,mn} &= f_{mn}(\rho), \\ h_{z,mn} &= H_{0,mn} f_{mn}(\rho), \end{aligned} \tag{A.16}$$

where

$$f_{mn}(\rho) = \begin{cases} \dfrac{J_m(\alpha_{c,mn}\rho)}{J_m(\alpha_{c,mn}a)} & \text{for} \quad r \le a \quad \text{(core)}, \\ \dfrac{H_m(\alpha_{b,mn}\rho)}{H_m(\alpha_{b,mn}a)} & \text{for} \quad r > a \quad \text{(background)}, \end{cases} \tag{A.17}$$

and

$$H_{0,mn} = \left(\frac{1}{\alpha_{c,mn}^2} - \frac{1}{\alpha_{b,mn}^2}\right) \frac{m\beta_{mn}}{ka\left(\dfrac{J_m'(\alpha_{c,mn}a)}{\alpha_{c,mn}J_m(\alpha_{c,mn}a)} - \dfrac{H_m'(\alpha_{b,mn}a)}{\alpha_{b,mn}H_m(\alpha_{b,mn}a)}\right)}. \tag{A.18}$$

The normalization constant A_{mn} for the β_{mn} mode is computed using the expression

$$A_{mn} = \sqrt{\frac{1}{-2\pi i L_{mn} + 4\pi\int_0^a \left(e_{r,mn}h_{\theta,mn} + e_{\theta,mn}h_{r,mn}\right) r\,dr}}, \tag{A.19}$$

where

$$L_{mn} = \left[h_{z,mn}\frac{\partial e_{\theta,mn}}{\partial \beta_{mn}} - e_{\theta,mn}\frac{\partial h_{z,mn}}{\partial \beta_{mn}} + e_{z,mn}\frac{\partial h_{\theta,mn}}{\partial \beta_{mn}} - h_{\theta,mn}\frac{\partial e_{z,mn}}{\partial \beta_{mn}}\right]_{r=a^+}. \tag{A.20}$$

Here, the term L is evaluated at $r = a^+$, i.e., on the background side of the core–background interface. This expression for A_{mn} follows from the bi-orthogonality condition of β_{mn} modes and ensures that it remains non-zero even for exponentially diverging leaky modes. The transverse components ($e_{r,mn}, e_{\theta,mn}$) and ($h_{r,mn}, h_{\theta,mn}$), required to evaluate (A.19), are obtained by substituting the axial components $e_{z,mn}$ and $h_{z,mn}$ into the expressions given in (A.9).

Appendix B. Slab waveguide

In this Appendix, we present the analytical derivatives of the transcendental equations associated with the general asymmetrically bound slab waveguide geometry, which are used in our root-search algorithm, along with the corresponding field profiles of the roots.

B.1. Derivatives of transcendental equations

We derive the derivatives of the transcendental equations for TE and TM modes in slab waveguide geometry with respect to the search variables $(\alpha_f a)^2$ and $(\beta a)^2$.

B.1.1. TE modes

For notational simplicity, we define

$$R^{\mathrm{TE}} = \frac{(\alpha_f a)^2 + (\alpha_c a)(\alpha_s a)}{\alpha_f a}, \tag{B.1}$$

so that the TE modes transcendental equation (7) becomes

$$f^{\mathrm{TE}} = R^{\mathrm{TE}}\tan(\alpha_f a) + i(\alpha_c a + \alpha_s a). \tag{B.2}$$

The derivative of f^{TE} with respect to $(\alpha_f a)^2$ is

$$\frac{\partial f^{\mathrm{TE}}}{\partial(\alpha_f a)^2} = \left(\frac{\partial R^{\mathrm{TE}}}{\partial(\alpha_f a)^2}\tan(\alpha_f a) + \frac{R^{\mathrm{TE}}}{2\alpha_f a}\sec^2(\alpha_f a)\right), \tag{B.3}$$

where

$$\frac{\partial R^{\mathrm{TE}}}{\partial(\alpha_f a)^2} = \frac{(\alpha_f a)^2 - (\alpha_c a)(\alpha_s a)}{2(\alpha_f a)^3}. \tag{B.4}$$

[3] These expressions for the transverse components are derived from Maxwell's equations in Gaussian units.

Next, we obtain the derivative of f^{TE} with respect to $(\beta a)^2$ as

$$\frac{\partial f^{\mathrm{TE}}}{\partial(\beta a)^2} = \left(-\frac{\partial R^{\mathrm{TE}}}{\partial(\alpha_f a)^2} - \frac{\partial R^{\mathrm{TE}}}{\partial(\alpha_c a)^2} - \frac{\partial R^{\mathrm{TE}}}{\partial(\alpha_s a)^2} \right) \tan(\alpha_f a) - \frac{R^{\mathrm{TE}}}{2\alpha_f a} \sec^2(\alpha_f a) + \frac{i}{2\alpha_c a} + \frac{i}{2\alpha_s a}, \tag{B.5}$$

where the chain rule was used along with the identity

$$\frac{\partial(\alpha_j a)^2}{\partial(\beta a)^2} = -1, \qquad j \in \{c, f, s\}. \tag{B.6}$$

In addition to (B.4), the remaining derivatives of R^{TE} used in (B.5) are

$$\frac{\partial R^{\mathrm{TE}}}{\partial(\alpha_c a)^2} = \frac{\alpha_s a}{2(\alpha_f a)(\alpha_c a)}, \qquad \frac{\partial R^{\mathrm{TE}}}{\partial(\alpha_s a)^2} = \frac{\alpha_c a}{2(\alpha_f a)(\alpha_s a)}. \tag{B.7}$$

B.1.2. TM modes

Similarly to the TE case, we define

$$R^{\mathrm{TM}} = \frac{(\alpha_f a)^2 \epsilon_c \epsilon_s + \epsilon_f^2 (\alpha_c a)(\alpha_s a)}{(\alpha_f a)\epsilon_f}, \tag{B.8}$$

so that the TM modes transcendental equation (9) becomes

$$f^{\mathrm{TM}} = R^{\mathrm{TM}} \tan(\alpha_f a) + i(\epsilon_c \alpha_s + \epsilon_s \alpha_c). \tag{B.9}$$

The derivative of f^{TM} with respect to $(\alpha_f a)^2$ is

$$\frac{\partial f^{\mathrm{TM}}}{(\alpha_f a)^2} = \left(\frac{\partial R^{\mathrm{TM}}}{\partial(\alpha_f a)^2} \tan(\alpha_f a) + \frac{R^{\mathrm{TM}}}{2\alpha_f a} \sec^2(\alpha_f a) \right), \tag{B.10}$$

where

$$\frac{\partial R^{\mathrm{TM}}}{\partial(\alpha_f a)^2} = \frac{1}{(\alpha_f a)\epsilon_f} \left[\epsilon_c \epsilon_s + (\alpha_c a)(\alpha_s a) \frac{\partial \epsilon_f^2}{\partial(\alpha_f a)^2} \right] - \frac{R^{\mathrm{TM}}}{2(\alpha_f a)^2} - \frac{R^{\mathrm{TM}}}{\epsilon_f} \frac{\partial \epsilon_f}{\partial(\alpha_f a)^2}. \tag{B.11}$$

From the relation $\alpha_f^2 + \beta^2 = k^2 \mu_f \epsilon_f$, it follows

$$\frac{\partial \epsilon_f}{\partial(\alpha_f a)^2} = \frac{1}{(ka)^2 \mu_f}, \qquad \frac{\partial \epsilon_f^2}{\partial(\alpha_f a)^2} = \frac{2\epsilon_f}{(ka)^2 \mu_f}. \tag{B.12}$$

Next, we obtain the derivative of f^{TM} with respect to $(\beta a)^2$ as

$$\frac{\partial f^{\mathrm{TM}}}{(\beta a)^2} = \left(-\frac{\partial R^{\mathrm{TM}}}{\partial(\alpha_f a)^2} - \frac{\partial R^{\mathrm{TM}}}{\partial(\alpha_c a)^2} - \frac{\partial R^{\mathrm{TM}}}{\partial(\alpha_s a)^2} \right) \tan(\alpha_f a) - \frac{R^{\mathrm{TM}}}{2\alpha_f a} \sec^2(\alpha_f a) + \frac{i\epsilon_c}{2\alpha_s a} + \frac{i\epsilon_s}{2\alpha_c a}, \tag{B.13}$$

where the chain rule was used along with the identity

$$\frac{\partial(\alpha_j a)^2}{\partial(\beta a)^2} = -1, \qquad j \in \{c, f, s\}. \tag{B.14}$$

In addition to (B.11), the remaining derivatives of R^{TM} used in (B.13) are

$$\frac{\partial R^{\mathrm{TM}}}{\partial(\alpha_c a)^2} = \frac{\epsilon_f(\alpha_s a)}{2(\alpha_f a)\alpha_c a}, \qquad \frac{\partial R^{\mathrm{TM}}}{\partial(\gamma_s a)^2} = \frac{\epsilon_f(\alpha_c a)}{2(\alpha_f a)\alpha_s a}. \tag{B.15}$$

B.2. Mode field profiles

In this Appendix, we define the explicit expressions for the mode field profiles of slab waveguide geometry and their corresponding normalization constants for eigenpermittivity (ϵ_f) and in-plane propagation constant (β) modes.

B.2.1. ϵ_f modes

For TE modes, the electric field is polarized along the y-direction (transverse to the plane of incidence, $x - z$), and its modal profile is expressed as

$$\boldsymbol{E}_n(x, z) = \hat{y}\, A_n^{\mathrm{TE}}\, u_n(x)\, e^{i\beta z}, \tag{B.16}$$

where $u_n(x)$ represents the transverse spatial variation of the mode, with its piecewise form given by

$$u_n(x) = \begin{cases} \cos(\phi_n^{\mathrm{TE}})\, e^{i\alpha_c x}, & \text{for } x > 0 \text{ (cover)}, \\ \cos\left(\alpha_{f,n} x + \phi_n^{\mathrm{TE}}\right), & \text{for } -a \le x \le 0 \text{ (film)}, \\ \cos\left(\alpha_{f,n} a - \phi_n^{\mathrm{TE}}\right)\, e^{-i\alpha_s (x+a)}, & \text{for } x < -a \text{ (substrate)}, \end{cases} \tag{B.17}$$

and the phase shift ϕ_n^{TE} is given by

$$\phi_n^{\mathrm{TE}} = \tan^{-1}\left(\frac{-i\alpha_c}{\alpha_{f,n}} \right). \tag{B.18}$$

The index n represents the n^{th} eigenpermittivity mode, and the normalization constant A_n^{TE} is given by

$$A_n^{\mathrm{TE}} = \frac{1}{\sqrt{\int_{-a}^{0} u_n^2(x) dx}} = \frac{1}{\sqrt{\frac{a}{2} + \frac{1}{2\alpha_{f,n}} \sin\left(\alpha_{f,n} a\right) \cos\left(\alpha_{f,n} a - 2\phi_n^{\mathrm{TE}}\right)}}. \tag{B.19}$$

This normalization expression follows from the bi-orthogonality condition of the eigenpermittivity modes.

For TM modes, since the electric field has nonzero components along both the x and z directions, it is standard to represent the mode profile in terms of the y-polarized magnetic field, i.e.,

$$\boldsymbol{H}_n(x, z) = \hat{y}\, A_n^{\mathrm{TM}}\, v_n(x)\, e^{i\beta z} \tag{B.20}$$

where the transverse spatial variation of the magnetic field, $v_n(x)$, is given by

$$v_n(x) = \begin{cases} \cos(\phi_n^{\mathrm{TM}})\, e^{i\alpha_c x}, & \text{for } x > 0, \\ \cos\left(\alpha_{f,n} x + \phi_n^{\mathrm{TM}}\right), & \text{for } -a \le x \le 0, \\ \cos\left(\alpha_{f,n} a - \phi_n^{\mathrm{TM}}\right)\, e^{-i\alpha_s (x+a)}, & \text{for } x < -a, \end{cases} \tag{B.21}$$

and the phase shift ϕ_n^{TM} is defined as

$$\phi_n^{\mathrm{TM}} = \tan^{-1}\left(\frac{-i\epsilon_{f,n}\, \alpha_c}{\epsilon_c\, \alpha_{f,n}} \right). \tag{B.22}$$

Using this magnetic field representation, the corresponding electric field vector for TM modes can be written as

$$E_n(x, z) = A_n^{\mathrm{TM}} e_n(x) e^{i\beta z}, \tag{B.23}$$

where the components of the transverse spatial variation vector, $e_n(x)$, in regions $j \in \{c, f, s\}$ is related to $v_n(x)$ as follows:

$$e_{x,n} = \frac{\beta}{k\epsilon_j} v_n(x), \quad e_{z,n} = \frac{i}{k\epsilon_j} \frac{\partial v_n(x)}{\partial x}. \tag{B.24}$$

The normalization constant A_n^{TM} is then determined based on the biorthogonality condition for the electric field, and is given by

$$A_n^{\mathrm{TM}} = \frac{1}{\sqrt{\int_{-a}^{0} \left(-e_{x,n}^2 + e_{z,n}^2 \right) dx}} = \frac{k\epsilon_{f,n}}{\sqrt{-\frac{k^2 \epsilon_{f,n} a}{2} + \left(\frac{\alpha_{f,n}^2 - \beta^2}{2\alpha_{f,n}} \right) \sin\left(\alpha_{f,n} a\right) \cos\left(\alpha_{f,n} a - 2\phi_n^{\mathrm{TM}}\right)}}. \tag{B.25}$$

B.2.2. β modes

Similarly, for TE modes with β eigenvalue, the electric field modal profile is given by

$$\boldsymbol{E}_n(x,z) = \hat{y}\, A_n^{\mathrm{TE}}\, u_n(x)\, e^{i\beta_n z}, \tag{B.26}$$

where

$$u_n(x) = \begin{cases} \cos(\phi_n^{\mathrm{TE}})\, e^{i\alpha_{c,n}x}, & \text{for } x > 0, \\ \cos\left(\alpha_{f,n}x + \phi_n^{\mathrm{TE}}\right), & \text{for } -a \le x \le 0, \\ \cos\left(\alpha_{f,n}a - \phi_n^{\mathrm{TE}}\right)\, e^{-i\alpha_{s,n}(x+a)}, & \text{for } x < -a, \end{cases} \tag{B.27}$$

and

$$\phi_n^{\mathrm{TE}} = \tan^{-1}\left(\frac{-i\alpha_{c,n}}{\alpha_{f,n}}\right). \tag{B.28}$$

The corresponding magnetic field vector for TE modes will be

$$H_n(x,z) = A_n^{\mathrm{TE}} h_n(x) e^{i\beta_n z}, \tag{B.29}$$

where the components of the transverse spatial variation vector, $h_n(x)$, in regions $j \in \{c, f, s\}$ is related to $u_n(x)$ as follows:

$$h_{x,n} = -\frac{\beta_n}{k\mu_j} u_n(x), \quad h_{z,n} = -\frac{i}{k\mu_j}\frac{\partial u_n(x)}{\partial x}. \tag{B.30}$$

Here, the index n represents the n^{th} eigenvalue of β, and the amplitude A_n^{TE} is the normalization constant of the n^{th} mode, given by

$$\begin{aligned} A_n^{\mathrm{TE}} &= \frac{1}{\sqrt{-i\left[h_{z,n}\frac{\partial u_n}{\partial \beta_n} - u_n\frac{\partial h_{z,n}}{\partial \beta_n}\right]_{x=-a^-}^{x=0^+} + 2\int_{-a}^{0} u_n(x) h_{x,n}\, dx}} \\ &= \frac{1}{\sqrt{-\frac{i\beta_n}{k\mu_c\alpha_{c,n}}u_n^2(0) - \frac{i\beta_n}{k\mu_s\alpha_{s,n}}u_n^2(-a) - \frac{2\beta_n}{k\mu_f}\int_{-a}^{0} u_n^2(x)\, dx}}. \end{aligned} \tag{B.31}$$

For TM modes, the mode profile is defined in terms of the y-polarized magnetic field, i.e.,

$$\boldsymbol{H}_n(x,z) = \hat{y}\, A_n^{\mathrm{TM}}\, v_n(x)\, e^{i\beta_n z}, \tag{B.32}$$

where

$$v_n(x) = \begin{cases} \cos(\phi_n^{\mathrm{TM}})\, e^{i\alpha_{c,n}x}, & \text{for } x > 0, \\ \cos\left(\alpha_{f,n}x + \phi_n^{\mathrm{TM}}\right), & \text{for } -a \le x \le 0, \\ \cos\left(\alpha_{f,n}a - \phi_n^{\mathrm{TM}}\right)\, e^{-i\alpha_{s,n}(x+a)}, & \text{for } x < -a, \end{cases} \tag{B.33}$$

and

$$\phi_n^{\mathrm{TM}} = \tan^{-1}\left[\frac{-i\epsilon_f\,\alpha_{c,n}}{\epsilon_c\,\alpha_{f,n}}\right]. \tag{B.34}$$

The corresponding electric field vector for TM modes will be

$$E_n(x,z) = A_n^{\mathrm{TM}} e_n(x) e^{i\beta_n z}, \tag{B.35}$$

where the components of the transverse spatial variation vector, $e_n(x)$, in regions $j \in \{c, f, s\}$ are related to $v_n(x)$ as follows:

$$e_{x,n} = \frac{\beta_n}{k\epsilon_j} v_n(x), \quad e_{z,n} = \frac{i}{k\epsilon_j}\frac{\partial v_n(x)}{\partial x}. \tag{B.36}$$

The normalization factor A_n^{TM} is given by

$$\begin{aligned} A_n^{\mathrm{TM}} &= \frac{1}{\sqrt{-i\left[-v_n\frac{\partial e_{z,n}}{\partial \beta_n} + e_{z,n}\frac{\partial v_n}{\partial \beta_n}\right]_{x=-a^-}^{x=0^+} + 2\int_{-a}^{0} e_{x,n}(x) v_n\, dx}} \\ &= \frac{1}{\sqrt{\frac{i\beta_n}{k\epsilon_c\alpha_{c,n}}v_n^2(0) + \frac{i\beta_n}{k\epsilon_s\alpha_{s,n}}v_n^2(-a) + \frac{2\beta_n}{k\epsilon_f}\int_{-a}^{0} v_n^2(x)\, dx}}. \end{aligned} \tag{B.37}$$

Appendix C. Permittivity normal modes of single sphere

In this Appendix, we present the analytical derivatives of the transcendental equations for a single spherical particle, which are used in our root-search algorithm, along with the corresponding mode field profiles and associated normalization constants for both TM and TE polarizations of the eigenpermittivity roots.

C.1. Derivatives of transcendental equation

In this subsection, we define the explicit expressions for the transcendental equations,

$$\frac{\partial f_l^{(\mathrm{TM})}(x)}{\partial x} = -\frac{j_\ell(x) j'_\ell(x) + x j_\ell(x)^2\left(1 - \frac{\ell(\ell+1)}{x^2}\right) + x\left(j'_\ell(x)\right)^2}{j_\ell(x)^2}, \tag{C.1}$$

and

$$\frac{\partial f_l^{(\mathrm{TE})}(x)}{\partial x} = \frac{-2 j_\ell(x) j'_\ell(x) - j'_\ell(x)\left(j_\ell(x) + x j'_\ell(x)\right)}{x^2 j_\ell(x)^2} + \frac{\ell(\ell+1)}{x^3} - \frac{1}{x} - \frac{2}{x^3}. \tag{C.2}$$

In this case, the analytical derivative of the transcendental equations with respect to x is simple (no need to apply the chain rule).

C.2. Mode field profiles

We now define the explicit expressions for the modes of a sphere using the radial function and the two basic types of the vector spherical harmonics (VSHs), transverse electric (TE) and transverse magnetic (TM) modes, i.e.,

$$\begin{aligned} TE &: \vec{E}_{nlm}^{(\mathrm{TE})}(\vec{r}) = f_{nl}^{(\mathrm{TE})}(r)\vec{X}_{lm}(\theta,\phi), \\ TM &: \vec{E}_{nlm}^{(\mathrm{TM})}(\vec{r}) = \frac{i}{k\left[1 - u_{nl}^{(\mathrm{TM})}\theta(r)\right]}\left[\nabla \times \left(f_{nl}^{(\mathrm{TM})}(r)\vec{X}_{lm}(\theta,\phi)\right)\right], \end{aligned} \tag{C.3}$$

where $\vec{X}_{lm}(\theta,\phi)$ is the vector spherical harmonics, and the radial function $f_{nl}^{(\mathrm{F})}$ for both $F = \mathrm{TE}, \mathrm{TM}$, takes the form

$$f_{nl}^{(F)}(r) = \begin{cases} A_{nl}^{(F)} j_l\left(k\left[1 - u_{nl}^{(F)}\right]^{1/2} r\right), & r < a, \\ B_{nl}^{(F)} h_l^{(1)}(k_b r), & r > a, \end{cases} \tag{C.4}$$

where $u_{nl}^{(F)} \equiv 1 - \epsilon_{nl}$. The continuity of $f_{nl}^{(\mathrm{TE})}$ ensures continuity of $H_\perp = H_r$ and the continuity of $\frac{df_{nl}^{(\mathrm{TE})}}{dr}$ ensures the continuity of $H_\parallel$.

Continuity of $f_{nl}^{(F)}$ dictates that

$$B_{nl}^{(F)} = A_{nl}^{(F)}\frac{j_l^{(1)}\left(x_{nl}^{(F)}\right)}{h_l^{(1)}(x_b)}, \tag{C.5}$$

where

$$x_{nl}^{(F)} \equiv k\left(1 - u_{nl}^{(F)}\right)^{1/2} a. \tag{C.6}$$

Now, demanding continuity of the parallel electric and magnetic field components, we get Eq. (10) and Eq. (11) from which we can determine the eigenvalues.

It is important to note that the dispersion relations depend on $ka = a\omega/c$, so that computing the eigenvalues for different particle sizes is equivalent to computing them for different frequencies.

C.3. Modes normalization

The coefficients $A_{nl}^{(F)}$ are determined from the normalization condition on $E_{nlm}^{(F)}$. For $F = TE$,

$$
\begin{aligned}
1 &= \langle C E_{nlm}^{(\mathrm{TM})} | E_{nlm}^{(\mathrm{TM})} \rangle = \int\limits_{r<a} d^3 r \left[A_{nl}^{(\mathrm{TM})} j_l \left(k \left(1 - u_{l,n}^{(\mathrm{TM})} \right)^{1/2} r \right) \right]^2 H_{lm}^* \cdot H_{lm}, \\
&= \left(A_{nl}^{(\mathrm{TM})} \right)^2 \int\limits_0^a r^2 dr \left[j_l \left(k \left(1 - u_{l,n}^{(\mathrm{TM})} \right)^{1/2} r \right) \right]^2 \\
&= \frac{\left(A_{nl}^{(\mathrm{TM})} \right)^2 a^3}{\left(x_{nl}^{(\mathrm{TM})} \right)^3} \int\limits_0^{x_{nl}^{(\mathrm{TM})}} dx x^2 \left[j_l(x) \right]^2, \\
&= \frac{\left(A_{nl}^{(\mathrm{TM})} \right)^2 a^3}{2 \left(x_{nl}^{(\mathrm{TM})} \right)^2} \left(\left[\psi_l' \left(x_{nl}^{(\mathrm{TM})} \right) \right]^2 + \left[\psi_l \left(x_{nl}^{(\mathrm{TM})} \right) \right]^2 - l(l+1) j_l^2 \left(x_{nl}^{(\mathrm{TM})} \right) - \right. \\
&\qquad \left. j_l \left(x_{nl}^{(\mathrm{TM})} \right) \psi_l' \left(x_{nl}^{(\mathrm{TM})} \right) \right).
\end{aligned} \tag{C.7}
$$

Here, $\psi_l(x) \equiv x j_l(x)$. Since H_{lm} is a Hermitian operator, its eigenstates, namely the VSHs, satisfy the usual orthogonality relations when integrated over the angular variables [6].
While for $F = TM$,

$$
\begin{aligned}
1 &= \langle C E_{nlm}^{(\mathrm{TE})} | E_{nlm}^{(\mathrm{TE})} \rangle \\
&= \left(\frac{i A_{nl}^{(\mathrm{TE})}}{k \left(\epsilon_{nl}^{(\mathrm{TE})} \right)} \right)^2 \int\limits_{r<a} d^3 r \left[\nabla \times j_l \left(k \left(\epsilon_{nl}^{(\mathrm{TE})} \right)^{1/2} r \right) H_{lm}^* \right] \\
&\quad \cdot \left[\nabla \times j_l \left(k \left(\epsilon_{nl}^{(\mathrm{TE})} \right)^{1/2} r \right) H_{lm} \right] \\
&= \frac{a^7 k^2}{\left(x_{nl}^{(\mathrm{TE})} \right)^7} \left(A_{nl}^{(\mathrm{TE})} \right)^2 \\
&\quad \cdot \int\limits_0^{x_{nl}^{(\mathrm{TE})}} \left(x^2 \left[l(l+1) + 1 \right] j_l^2(x) + \left[x j_l'(x) j_l(x) \left(2 + \frac{x j_l'(x)}{j_l(x)} \right) \right] \right) dx.
\end{aligned}
$$

Thus,

$$
\begin{aligned}
1 = \frac{a^5 k^2 \left(A_{nl}^{(\mathrm{TE})} \right)^2}{2 \left(x_{nl}^{(\mathrm{TE})} \right)^4} \Bigg(& \left[\psi_l' \left(x_{nl}^{(\mathrm{TE})} \right) \right]^2 + \left[\psi_l \left(x_{nl}^{(\mathrm{TE})} \right) \right]^2 \\
& - l(l+1) j_l^2 \left(x_{nl}^{(\mathrm{TE})} \right) + j_l \left(x_{nl}^{(\mathrm{TE})} \right) \psi_l' \left(x_{nl}^{(\mathrm{TE})} \right) \Bigg).
\end{aligned} \tag{C.8}
$$

We note that the orthogonalization integrals extend to the sphere volume only. The Bessel function integrals coincide with the available formula for integrals over the Bessel functions below [42]. We get

$$
\int\limits_0^{x_{nl}^{(F)}} y^2 j_l^2(y) dy = \tag{C.9}
$$

$$
= \frac{x_{nl}^{(F)} \left(\left[\psi_l' \left(x_{nl}^{(F)} \right) \right]^2 + \left[\psi_l \left(x_{nl}^{(F)} \right) \right]^2 - l(l+1) j_l^2 \left(x_{nl}^{(F)} \right) - j_l \left(x_{nl}^{(F)} \right) \psi_l' \left(x_{nl}^{(F)} \right) \right)}{2},
$$

$$
\int\limits_0^{x_{nl}^{(F)}} \left[\psi_l'(y)^2 + l(l+1) j_l^2(y) \right] dy = \tag{C.10}
$$

$$
= \frac{x_{nl}^{(F)} \left(\left[\psi_l' \left(x_{nl}^{(F)} \right) \right]^2 + \left[\psi_l \left(x_{nl}^{(F)} \right) \right]^2 - l(l+1) j_l^2 \left(x_{nl}^{(F)} \right) + j_l \left(x_{nl}^{(F)} \right) \psi_l' \left(x_{nl}^{(F)} \right) \right)}{2}.
$$

An alternative expression for these integrals is given in [22], which is expected to be numerically equivalent.

Data availability

No data was used for the research described in the article.

References

[1] P.Y. Chen, Y. Sivan, Robust location of optical fiber modes via the argument principle method, Comput. Phys. Commun. 214 (2017) 105–116.
[2] P. Yeh, Optical Waves in Layered Media, 2nd edition, Wiley-Interscience, 2005.
[3] K. Okamoto, Fundamentals of Optical Waveguides, 2nd edition, Academic Press, 2006.
[4] Q. Bai, M. Perrin, C. Sauvan, J.-P. Hugonin, P. Lalanne, Efficient and intuitive method for the analysis of light scattering by a resonant nanostructure, Opt. Express 21 (2013) 27371.
[5] D. Bergman, D. Stroud, in: H. Ehrenreich, D. Turnbull (Eds.), Solid State Physics, vol. 46, Academic Press, 1992, pp. 148–270.
[6] D.J. Bergman, D. Stroud, Theory of resonances in the electromagnetic scattering by macroscopic bodies, Phys. Rev. B 22 (1980) 3527–3539.
[7] T. Sandu, Eigenmode decomposition of the near-field enhancement in localized surface plasmon resonances of metallic nanoparticles, Plasmonics 8 (2012) 391–402.
[8] N. Liver, A. Nitzan, K.F. Freed, Radiative and nonradiative decay rates of molecules adsorbed on clusters of small dielectric particles, J. Chem. Phys. 82 (1985) 3831.
[9] N. Liver, A. Nitzan, J. Gersten, Local fields in cavity sites of rough dielectric surfaces, Chem. Phys. Lett. 111 (1984) 449–454.
[10] M.S. Agranovich, B.Z. Katsenelenbaum, A.N. Sivov, N.N. Voitovich, Generalized Method of Eigenoscillations in Diffraction Theory, Wiley-VCH, 1999.
[11] K. Li, M. Stockman, D. Bergman, Enhanced second harmonic generation in a self-similar chain of metal nanospheres, Phys. Rev. B 72 (2005) 153401.
[12] A.D.S. Li Ge, Y.D. Chong, Steady-state ab initio laser theory: generalizations and analytic results, Phys. Rev. A 82 (2010) 063824.
[13] O. Schnitzer, Singular perturbations approach to localized surface-plasmon resonance: nearly touching metal nanospheres, Phys. Rev. B 92 (2015) 235428.
[14] O. Schnitzer, V. Giannini, S.A. Maier, R.V. Craster, Surface plasmon resonances of arbitrarily shaped nanometallic structures in the small-screening length limit, Proc. Royal Soc. A 472 (2016) 20160258.
[15] A. Farhi, D. Bergman, Electromagnetic eigenstates and the field of an oscillating point electric dipole in a flat-slab composite structure, Phys. Rev. A 93 (2016) 063844.
[16] P.Y. Chen, D.J. Bergman, Y. Sivan, Generalizing normal mode expansion of electromagnetic Green's tensor to lossy resonators in open systems, Phys. Rev. Appl. 11 (2019) 044018.
[17] P.Y. Chen, Y. Sivan, E.A. Muljarov, An efficient solver for the generalized normal modes of non-uniform open optical resonators, J. Comput. Phys. 422 (2020) 109754.
[18] N. Kossowski, P.Y. Chen, Q.J. Wang, P. Genevet, Y. Sivan, Generalized normal modes of an anisotropic scatterer, J. Appl. Phys. 129 (2021) 113104.
[19] P.Y. Chen, Y. Sivan, Resolving Gibbs phenomenon via a discontinuous basis in a mode solver for open optical systems, J. Comput. Phys. 429 (2021) 110004.
[20] G. Rosolen, P.Y. Chen, B. Maes, Y. Sivan, Overcoming the bottleneck for quantum computations of complex nanophotonic structures: Purcell and Förster resonant energy transfer calculations using a rigorous mode-hybridization method, Phys. Rev. B 101 (2020) 155401.
[21] G. Rosolen, B. Maes, Strong multipolar transition enhancement with graphene nanoislands, APL Photon. 6 (2021) 086103.
[22] C. Forestiere, G. Miano, Material-independent modes for electromagnetic scattering, Phys. Rev. B 94 (2016) 201406.
[23] M. Pascale, G. Miano, C. Forestiere, Spectral theory of electromagnetic scattering by a coated sphere, J. Opt. Soc. Am. B 34 (7) (2017) 1524–1535.
[24] C. Forestiere, G. Miano, G. Rubinacci, A. Tamburrino, R. Tricarico, S. Ventre, Volume integral formulation for the calculation of material independent modes of dielectric scatterers, IEEE Trans. Antennas Propag. 66 (2018) 2505.
[25] M. Pascale, G. Miano, R. Tricarico, C. Forestiere, Full-wave electromagnetic modes and hybridization in nanoparticle dimers, Sci. Rep. 9 (2019).
[26] S. Rao, P.Y. Chen, G. LeSaux, Y. Sivan, Generalised normal mode expansion method for open and lossy periodic structures, J. Opt. Soc. Am. B 39 (2022) 1338–1347.
[27] P.Y. Chen, Y. Greenberg, Y. Sivan, Wide frequency band expansion of permittivity normal modes, J. Opt. Soc. Am. B 39 (2022) 2387–2394.
[28] G.Y. Slepyan, D. Mogilevtsev, I. Levie, A. Boag, Modeling of multimodal scattering by conducting bodies in quantum optics: the method of characteristic modes, Phys. Rev. Appl. 18 (2022) 014024.
[29] N. Moiseyev, Non-hermitian Quantum Mechanics, Cambridge University Press, 2011.
[30] W. Chew, Waves and Fields in Inhomogeneous Media, Wiley-IEEE Press, 1999.
[31] D. Marcuse, Theory of Dielectric Optical Waveguides, Academic, 1972.
[32] M. Abramowitz, I. Stegun, Handbook of Mathematical Functions, Dover Publications, New York, 1965.

[33] F. Betz, F. Binkowski, J.D. Fischbach, N. Feldman, L. Zschiedrich, C. Rockstuhl, A.F. Koenderink, S. Burger, Uncovering hidden resonances in non-Hermitian systems with scattering thresholds, arXiv preprint, arXiv:2503.03549, 2025.

[34] P. Lalanne, W. Yan, K. Vynck, C. Sauvan, J.-P. Hugonin, Light interaction with photonic and plasmonic resonances, Lasers Photon. Rev. 12 (2017) 1700113.

[35] E.A. Muljarov, W. Langbein, R. Zimmermann, Brillouin-Wigner perturbation theory in open electromagnetic systems, Europhys. Lett. 92 (2010) 50010.

[36] F.J. García de Abajo, Nonlocal effects in the plasmons of strongly interacting nanoparticles, dimers, and waveguides, J. Phys. Chem. C (2008) 17983–17987.

[37] S. Raza, G. Toscano, A.-P. Jauho, M. Wubs, N.A. Mortensen, Unusual resonances in nanoplasmonic structures due to nonlocal response, Phys. Rev. B 84 (2011) 121412(R).

[38] N.A. Mortensen, S. Raza, M. Wubs, T. Sondergaard, S.I. Bozhevolnyi, A generalized non-local optical response theory for plasmonic nanostructures, Nat. Commun. 5 (2014) 3809.

[39] Y. Luo, R. Zhao, J. Pendry, Van der Waals interactions at the nanoscale: the effects of nonlocality, Proc. Natl. Acad. Sci. USA 111 (2014) 18422–18427.

[40] A.I. Fernández-Domímguez, A. Wiener, F.J. Garcia-Vidal, S.A. Maier, J.B. Pendry, Transformation-optics description of nonlocal effects in plasmonic nanostructures, Phys. Rev. Lett. 108 (2012) 106802.

[41] H. Du, W. Wang, C. Liu, Nonlocal optical response in asymmetric imi plasmonic waveguides, Micro Nanostruct. 188 (2024) 207784.

[42] R. McPhedran, B. Stout, “Killing mie softly”: analytic integrals for resonant scattering states, arXiv preprint, arXiv:1811.07132, 2018.